

A new method for structural diagnostics with muon tomography and deep learning

Lorenzo Pezzotti^{*1}, Davide Cifarelli², Daniele Corradetti^{3,4}, José Paulo Costa⁴, Antonio Gallerati⁵, Lorenzo Galante⁵, Giorgio Gabrielli², Ivan Gnesi^{6,7,8,9}, Alessio Marrani^{2,7}

¹Istituto Nazionale di Fisica Nucleare, Sez. Bologna, viale Carlo Berti Pichat 6/2, 40127 Bologna, Italy

²Elementar, Divisione Ricerca e Sviluppo, Galleria Enzo Tortora 21, 10121 Torino, Italy

³Grupo de Física Matemática, Instituto Superior Técnico, Av. Rovisco Pais, 1049-001, Lisboa, Portugal

⁴STAP Reabilitação Estrutural, SA Rua General Ferreira Martins 8 - 9B, Algés, 1495-137, Portugal

⁵Politecnico di Torino, corso Duca degli Abruzzi 24, 10129 Torino, Italy

⁶Centro Ricerche Enrico Fermi, piazza del Viminale 1, 00184 Roma, Italy

⁷Dipartimento di Management “Valter Cantino”, Corso Unione Sovietica 218 Bis, 10134, Torino, Italy

⁸INFN - Laboratori Nazionali di Frascati, Via Enrico Fermi 54, 00044 Frascati, Italy

⁹CERN, 1211 Geneva 23, Switzerland

Abstract

This work investigates the production of high-resolution images of typical support elements in concrete structures by means of the muon tomography (muography). By exploiting detailed Monte Carlo radiation-matter simulations, we demonstrate the feasibility of the reconstruction of 1 cm-thick iron tubes inside 30 cm-deep concrete blocks, regarded as an important testbed within the structural diagnostics community. In addition, we present a new method for integrating simulated data with advanced deep learning techniques in order to improve the muon imaging of concrete structures. Through deep learning enhancement techniques, this results in a dramatic improvement of the image quality and a significant reduction of the data acquisition time, which are two critical limitations within the usual practice of muography for civil engineering diagnostics.

^{*}lorenzo.pezzotti@cern.ch

Contents

1	Introduction	3
2	Methodology overview	5
3	GEANT4 simulations and analytical results	6
3.1	Simulation design and strategy	6
3.2	Data analysis and results	8
3.3	Relevance of the detector spatial resolution	10
4	Neural network algorithm development	11
4.1	Dataset augmentation pipeline	11
4.2	Neural network architecture	15
4.2.1	U-Net architecture with RRDB	15
4.2.2	Detailed network configuration	15
4.2.3	Hyperparameter selection	18
4.3	Training process	18
4.3.1	Loss function and optimization algorithm	20
5	Results	20
5.1	Analysis of the quality metrics	21
5.2	Visual comparisons and qualitative analysis	24
6	Conclusion	25
	References	28

1 Introduction

Muon imaging is a well-known non-invasive technique exploiting cosmic ray muons to investigate the internal structure of dense objects. Muons are elementary particles created when cosmic rays interact with atoms in the Earth’s atmosphere, generating showers of secondary particles which, traveling at nearly the speed of light, reach the Earth’s ground and further cross wide thicknesses of matter. This continuous shower of muonic particles makes them highly effective for probing dense materials, usually impenetrable to other types of radiation, such as X-rays [1].

The main idea at the core of muon imaging is to detect the attenuation or scattering of muons as they move through a medium. As intuitively reasonable, denser regions, i.e. regions with a higher density of the budget material, give rise to a greater attenuation or scattering, which can then be mapped in order to reveal the internal structure of the traversed objects. Remarkably, this crucial feature of muonic fluxes found application in a variety of contexts, ranging from archaeology [2–4], to geophysics [5–7], nuclear waste management [8, 9], and civil engineering [10].¹

Within the field of civil engineering, the diagnostics of concrete structures provides a natural framework for the application of muon tomography (usually named muography). In fact, this context is plagued by the increasing issue of the aging of concrete structures: as time passes, bridges, tunnels, and historic buildings constructed throughout the 20th century are all reaching the end of their planned lifetime [12, 13]. A faithful assessment of the state of concrete structures is often hindered by the lack of a complete or accurate technical documentation on the structure themselves; the original construction projects are often missing, so that even a basic information on the original structural configuration and matter composition is not available [14, 15]. Unfortunately, traditional probing methods, such as ground-penetrating radar (GPR), ultrasound techniques and infrared thermography, are mostly ineffective and inaccurate when dealing with dense and thick materials, like reinforced concrete [16, 17]. Indeed, GPR typically penetrates the concrete until a depth of at most 2 meters only, and it has major issues when dealing with multiple reinforcement layers. On the other hand, ultrasonic methods work fine for detecting cracks, but quickly become ineffective as the thickness of the concrete increases. Finally, infrared thermography can pro-

¹ For a complete review and a list of references, see e.g. [11].

vide information about the state of surface layers, but says nothing about possible internal voids or defects.

The aforementioned problems can be effectively dealt with by muography, especially for what concerns the depth of penetration and energy efficiency [18]. However, of course, muography comes with its own limitations: while being more penetrative, it can suffer from poor spatial resolution, caused by the scattering of muons. For instance, the horizontal resolution of typical muon imaging systems is strongly constrained by the geometry and angular acceptance of the detectors [5], whereas the vertical resolution suffers from quite severe limitations due to the natural angular distribution of cosmic ray muons, which suffer from an horizontal bias causing anisotropic imaging artifacts [10]. Also, an important limit of muography is the time required to reach a number of detections of muons large enough to grant for images with acceptably high resolution. In fact, the muon flux at sea level is approximately 170 particles per square meter per second [19], while, within standard techniques, millions of muons are needed to generate statistically meaningful images [10]. This results in data acquisition times that range from days to weeks and makes muography too cumbersome and essentially unpractical; for example, diagnosing an infrastructure such as a bridge would require a service interruption of several days, which is usually not an option.

In order to address the problems described above, in the present paper we propose a new setup integrating GEANT4, the state-of-the-art simulation toolkit for particle interactions with matter [20–22], along with an image enhancement through deep learning which exploits standard data segmentation techniques combined with U-Nets with residual dense blocks. On the one hand, by means of muonic simulations, we will investigate the spatial resolution issue within the analysis of reinforced concrete structures. On the other hand, by training neural networks on simulated datasets, we will be able to significantly reduce the amount of muon events needed to reconstruct a meaningful image.

The paper is developed according to the following structure. Section 2 introduces the methodology, presenting the integration of GEANT4 simulations with neural network models. Section 3 deals with the design and implementation of the simulations, providing a detailed treatment of the key parameters, as well as of the analytical results obtained. Then, Section 4 pertains to the development of neural network algorithms, focusing on architecture, data augmentation techniques, and training procedures. A detailed discussion of the results, including both quantitative and qualitative evaluations of the reconstructed images, is provided in

Section 5. Finally, in Section 6 we conclude with a summary of our findings, with an outlook of potential directions for future researches and applications.

2 Methodology overview

The methodology proposed in this paper makes use of GEANT4 simulations for modeling the interaction of muons with reinforced concrete, generating synthetic data to train neural networks aimed at enhancing image resolution and reducing noise.

As the first step, detailed GEANT4 simulations are developed and executed, in order to model the passage of muons through concrete structures containing iron reinforcements. GEANT4 is a Monte Carlo toolkit for the simulation of muon interactions with matter, considering all possible physical processes such as ionization, multiple scattering, and bremsstrahlung. For this study, our preliminary objective was to determine the feasibility of identifying iron cylinders with a diameter of 10 mm embedded in a $30 \times 30 \times 30 \text{ cm}^3$ concrete cube, arranged in various configurations. This geometric setup was considered fundamental by our engineering consultants, in view of further specialized developments in structural diagnostics. Clearly, different practical scenarios – such as bridge diagnostics with beams and pre-stressing cables, water tanks, and underwater structures – will require different simulations to generate synthetic data aligned with the structures under examination. For the present preliminary feasibility study, muons are generated in the simulation with energies between 3 and 4 GeV, uniformly distributed over the surface of the concrete block. Two detection planes, placed 1 m upstream and downstream of the block, recorded the positions of the muons before and after interacting with the sample. Then, the deflection angles of the muon tracks undergo a detailed analysis, in order to infer the presence and position of the iron cylinders within the concrete.

Once a large simulation dataset pertaining to the structure being diagnosed has been produced, the second step is to develop the deep learning models to improve the data obtained from the simulations. In this investigation, our priority is to reconstruct high-resolution images from datasets with a limited number of muon events. This can be achieved by applying U-Net architectures enriched with residual-in-residual dense blocks (RRDB), known for their effectiveness in super-resolution tasks [23, 24]. Although reducing the number of muon events was our primary goal, as demonstrated in Section 5, the proposed architecture

also achieves a significant and visible reduction in the signal-to-noise ratio.

Once the network architecture is established, the third step consists of the use of the simulated data from GEANT4 as input for the neural network training. These datasets are subjected to data augmentation techniques, including rotations, reflections and flips, in order to expand the training data and to improve the model generalization.

Thus, by integrating analytical reconstruction techniques with deep learning models, our methodology achieves two key results while bringing muography into civil engineering practice. Firstly, it allows for the reconstruction of internal iron structures even from datasets with a limited number of muon events: as shown in Section 5, inference on images derived from 10^5 muon events yields to results comparable to images derived from 4.5×10^6 events. Secondly, the background noise resulting from the event variability gets naturally smoothed: this feature is explicitly measured by the Gradient Magnitude Similarity Deviation (GMSD) metric when compared to Ground Truth, as discussed in Section 5.

All in all, this work demonstrates that the combination of GEANT4 simulations and deep learning techniques gives rise to a remarkably effective approach to the enhancement of the spatial resolution and accuracy of muography, paving the way to a number of potential applications in non-invasive monitoring of complex engineering structures.

3 GEANT4 simulations and analytical results

3.1 Simulation design and strategy

To address the possibility of reconstructing the metallic support structure inside concrete elements, we performed detailed comprehensive simulations of the interaction of negatively charged muons in several sample structures. To this aim, we made use of the GEANT4 software [20–22] (release 11.1.0); this is a multi-purpose simulation toolkit for Monte Carlo simulations of radiation-matter interactions. In particular, GEANT4 allows for the tracking of any particle in any material with great accuracy, taking into account that the vast majority of interaction processes ranges in energy from hundreds of TeV down to thermal energies. For these reasons, GEANT4 is currently a gold standard for simulations of particles interacting with matter in nuclear, high-energy, biomedical and atmospheric physics.

The complete simulation software to study the motion of muons across reinforced concrete structures was designed as a C++ code on the GEANT4 library.

In this project, our main goal was to investigate the possibility of detecting and resolving metal structures immersed in concrete blocks. The concrete block had a common geometry, namely a $30 \times 30 \times 30 \text{ cm}^3$ cube. The composition of the concrete was a mixture of the following elements and mass fractions: H (1.0%), C (0.1%), O (52.91%), Na (1.6%), Mg (0.2%), Al (3.39%), Si (33.70%), K (1.39%), Ca (4.40%), Fe (1.4%). Moreover, the concrete density was set at 2.3 g/cm^3 and its radiation length to 11.55 cm. The concrete block was placed at the origin $\mathcal{O} = (0, 0, 0)$ of a standard right-handed reference frame, and it was considered to be immersed in the Earth's atmosphere, at standard temperature, pressure and density.

Inside the concrete block, cylindrical iron tubes of 1 cm diameter and 25 cm length were placed in random positions, parallel to the x or z axes. In this framework, the density of the iron was set to 7.874 g/cm^3 , and its radiation length to 1.757 cm. By placing a random number of tubes from 0 to 15 inside the concrete block, a sample geometry was defined; for instance, Fig. 1 (left) shows a sample geometry, in which two iron tubes are inserted. Then, We simulated a total of 100 sample geometries and, for each geometry, we verified the absence of non-physical overlaps among the tubes. This provided us with a set of geometries, which we were subsequently going to employ for analytical and machine learning studies.

For what concerns muons, we simulated a muon radiation source consisting of negatively charged muons, traveling along the direction $\text{Dir} = (0, -1, 0)$ and uniformly distributed over the face of the concrete block parallel to the xz plane, with positive y coordinate. To prevent muons from entering the block structure too close to its edges and thus possibly undergoing a scattering out of the sample, the impact points of muons were distributed on a surface of $28 \times 28 \text{ cm}^2$ at the geometric center of the front face of the concrete block. Furthermore, the kinetic energy of the muons was simulated to be uniformly distributed in the range 3 – 4 GeV, similar to the case in which the sample is exposed to accelerator particle beams. Fig. 1 (right) provides a graphical representation of the interaction of five muon tracks (in red) within one sample geometry.

Our simulations tracked each primary muon through the sample, thus recording one event per each primary muon. The tracking of muons in the simulation took into account every relevant physical process involved into muonic interactions within matter, like ionization, multiple scattering, bremsstrahlung, and

lepto-nuclear interactions, as they are modelled within the FTTP_BERT GEANT4 Physics List, which is recommended for high-energy physics simulations.

In order to record the muon position before and after its interaction within the sample, two detecting planes, parallel to the xz plane, were included in the simulation, and posited 1 m before the sample’s front face and 1 m after its rear face. When a muon track propagated through such planes, the (x, z) coordinates were stored in files for later analysis. In the case in which the muon track did not reach the downstream detector plane, for instance because it induced a nuclear breakup in the sample geometry via the lepto-nuclear effect, we decided to neglect the event within our data analysis.

The dataset employed for our investigation consisted of 18×10^6 events for each sample geometry, thus delivering a realistic set of synthetic data to address the possibility of resolving metallic support structures within concrete structures. In the case in which the muons traveled along the y -direction, only the projective image along this direction could be resolved, resulting in a two-dimensional figure in the xz plane. Fig. 2 shows the actual y -projection for the sample shown in Fig. 1, and it represents the target for the subsequent analyses. Indeed, it shows the number of tubes inside the concrete structure (left) and the corresponding material budget map in radiation lengths X_0 (right). The relative budget material increases from $2.6 X_0$ for the areas covered by concrete only, to $2.68 X_0$ (+3%) for the areas covering only one iron tube, to $2.75 X_0$ (+6%) for the areas covering two iron tubes.

3.2 Data analysis and results

The Monte Carlo data stored for offline analysis consisted of two vectors, containing the position of the primary muon track crossing the upstream detector plane (Pos_1), as well as the downstream detector plane (Pos_2). The properties of the secondary particles produced by the muonic interaction within the samples were not considered in the analysis.

The crucial quantity exploited in the resolution of the metallic structures was the Root Mean Square (RMS) of the muon tracks deflection angle. Within the energy range under consideration, this angle is almost uniquely due to the multiple scattering of charged particles within the electric field of the nuclei in the concrete block. In order to determine it, after calculating the vector $\text{Track} = \text{Pos}_2 - \text{Pos}_1$, we computed its angle with the original muon directions $\text{Dir} = (0, -1, 0)$ as the arc-cosine of the dot product of the normalized Track and Dir vectors. The

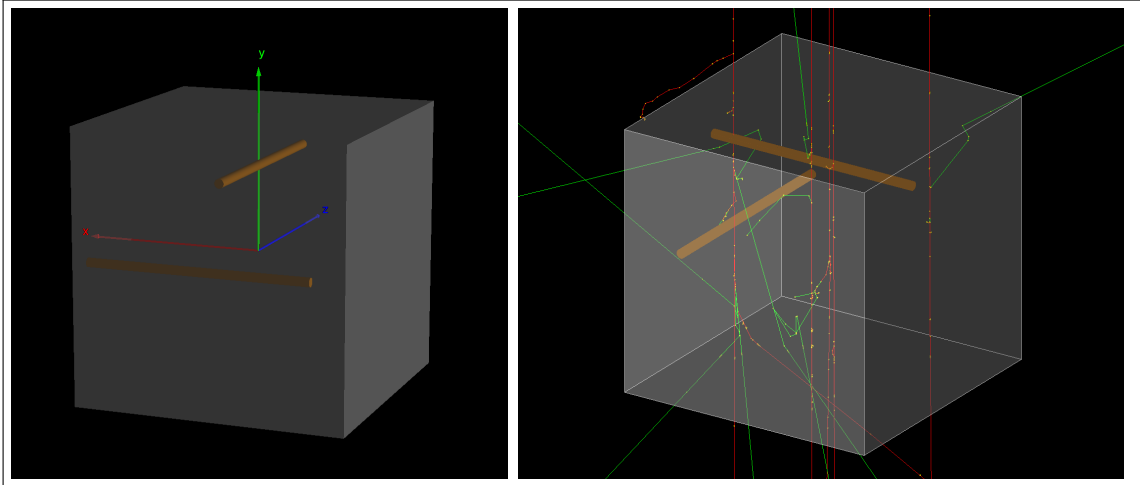


Figure 1: A simulated sample geometry, consisting of a concrete block housing two iron tubes (left). Simulated interactions of five muons (red tracks), including the generation of secondary particles (green tracks) in the same geometry sample (from the GEANT4 simulation).

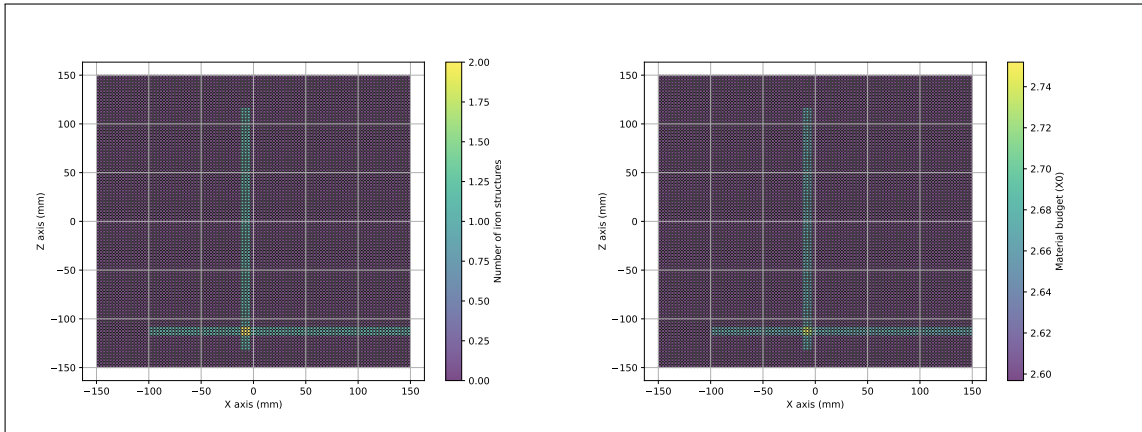


Figure 2: Projections along the y -direction of the iron tubes content inside the sample geometry shown in Fig. 1 (left), and of the effective budget material in radiation lengths X_0 (right).

resulting angle is therefore the scattering angle experienced by muons over a 2.3 meter distance: 1 meter of air plus 0.3 m of concrete, with an additional meter of air downstream.

We divided the front face of the sample geometry into $1 \times 1 \text{ mm}^2$ pixels and

collected the distributions of the scattering angle for muons entering each pixel separately. This procedure defined 280×280 pixels, corresponding to an equal number of angular distributions. While using 18×10^6 muon events per sample, each pixel was crossed on average by 230 muons. Per each pixel, we extracted the scattering angle RMS from the corresponding distribution. The result for the geometry sample of Fig. 1 is shown in Fig. 3, and it should be compared with the true y -projection of the sample shown in Fig. 2: it is easy to appreciate the effectiveness of muon tomography for high-resolution images of metallic structures within concrete blocks, and its potentially successful applicability in monitoring civil engineering constructions.

Two important limitations of the approach outlined above will be considered in the following sections. We will discuss the impact of the detector spatial resolution on the imaging capability in Subsec. 3.3, whereas in Sec. 4 we will discuss the need to expose the sample under study to a very high number of muon events in order to achieve high-resolution images.

3.3 Relevance of the detector spatial resolution

The treatment outlined above did not take into account a realistic resolution in the detection of muon tracks passing through the upstream and downstream detecting layers. In order to address the importance of the spatial resolution of such detectors, we repeated the data analysis while applying a uniform smearing on the Pos_1 and Pos_2 , x and z coordinates. This smearing was applied by drawing a uniformly distributed random number within \pm the expected detector resolution and subsequently adding it to the measured coordinate. Four independent random numbers were generated for each event, according to a hypothetical resolution, and applied to the data. We considered resolutions of 5, 10 and 20 mm. It should be noted that the impact of the detector resolution on the imaging results is twofold, since it introduces an error in the association of the muon track to the correct pixel and it also worsens the resolution on the measurement of the muon scattering angle.

Fig. 4 shows the imaging along the y -direction for the sample analysed above. We would like to stress that the inclusion of a 5 mm smearing to planar detectors, placed at a 1 m distance from sample front and back faces, did not affect the high-resolution capability of this technique (top). Signs of image deterioration emerged when considering a resolution of 10 mm (middle), and no internal structures were resolvable at all with a spatial resolution of 20 mm (bottom). It should be

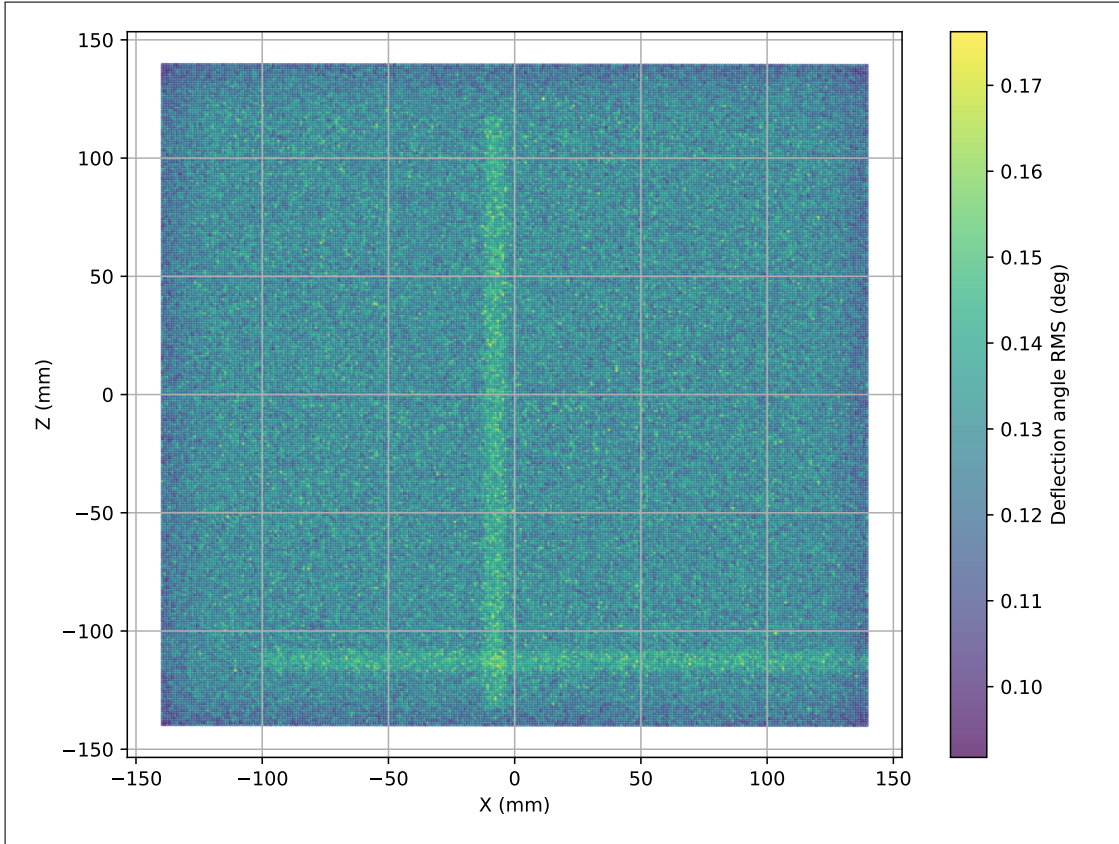


Figure 3: Scatter plot of the deflecting angle RMS of muon tracks passing through the sample geometry shown in Fig. 1 and travelling along the y -direction. The image has been created by grouping muon tracks into 1 mm^2 pixels.

remarked that the spatial resolution requirement is well within the reach of several particle trackers, like large-area silicon sensors, micro-pattern gas detectors, and optical fibers-based tracking systems.

4 Neural network algorithm development

4.1 Dataset augmentation pipeline

The generation of synthetic data by GEANT4 is computationally intensive; therefore, we developed a pipeline that magnifies dataset size by a factor of 80, by exploiting data augmentation techniques such as rotations and reflections. Let us recall that data augmentation not only enlarges the dataset, but also often

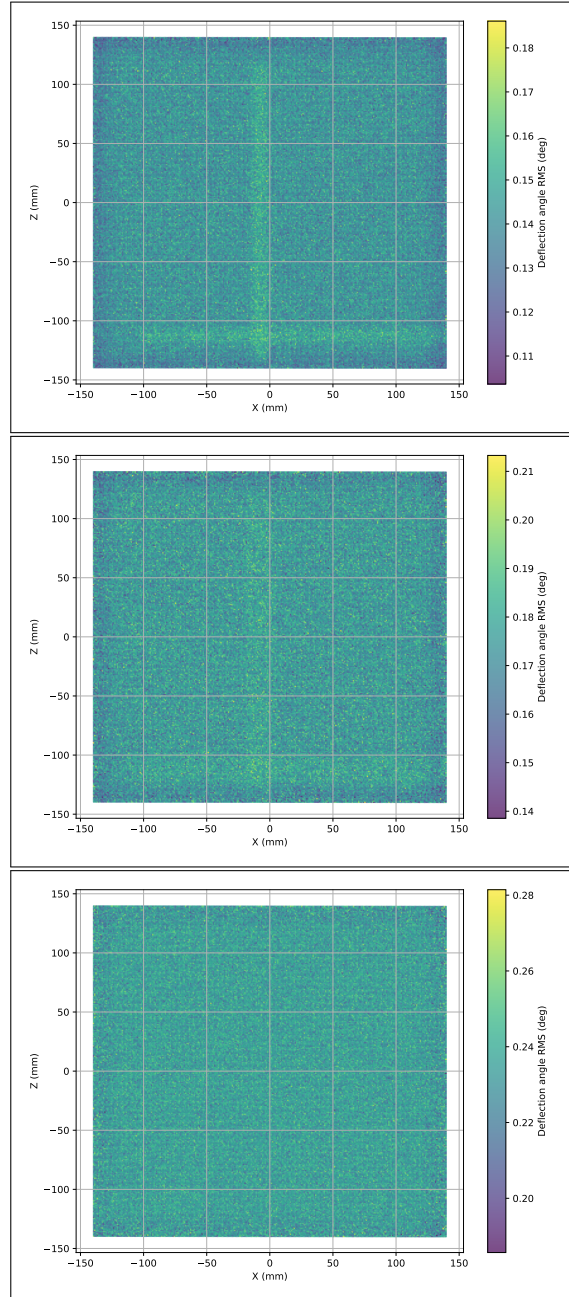


Figure 4: Scatter plots of the deflecting angle RMS of muon tracks passing through the sample geometry shown in Fig. 1, and travelling along the y -direction. The images have been created with a spatial resolution for both detecting planes of 5 (up), 10 (middle), and 20 (bottom) mm; see the text for details.

improves the generality of the model, since it provides diverse representations of the data. In this context, we split each element of the dataset \mathcal{D} generated by GEANT4 into four distinct quadrants, based on the coordinates x_0 and z_0 . After removing incomplete events (i.e., those in which the muons pass through one or more detectors without activating all of them), the original dataset \mathcal{D}_0 is defined as

$$\mathcal{D}_0 = \left\{ (\mathcal{G}_k, \mathcal{E}_k)_{k=1, \dots, 100} \right\}. \quad (1)$$

Since the dataset \mathcal{D} was generated with 100 geometries, the original dataset \mathcal{D}_0 comprises 400 geometries \mathcal{G}_k , and each of them is associated to a collection of muon events \mathcal{E}_k , with $k = 1, \dots, 400$. Each \mathcal{E}_k consists of 4.5×10^6 muonic events, with each event recorded as four triplets (x, y, z) representing the coordinates of detectors 1 through 4 crossed by the muon. Specifically, it holds that

$$\mathcal{E}_k = \left\{ (x_i, y_i, z_i)_{i=1, \dots, 4} : x_i \in [-75, 75], y_i \in \{y_1, \dots, y_4\}, z_i \in [-75, 75], \right\}. \quad (2)$$

Therefore, each element of the original dataset undergoes the following transformations:

- i) 90° , 180° , and 270° rotations of the data;
- ii) 12 additional rotations in increments of 30° , i.e., 30° , 60° , 120° , etc.;
- iii) a reflection across the vertical axis;
- iv) a reflection across the horizontal axis;
- v) finally, a reflection through both the horizontal and vertical axes.

In this way, the Augmented Dataset \mathcal{D}_A contains 7600 samples consisting of a Geometry \mathcal{G}_k , each with 4.5×10^6 events \mathcal{E}_k .

Starting from the Augmented Dataset \mathcal{D}_A , four datasets for neural network training are created. Specifically, for a given pixel resolution, all events corresponding to the coordinates of the same pixel get grouped together. From such data, the difference in position between the various detectors is calculated, together with the mean of the absolute value of the deflection angle, the covariance and the correlation between x and y , the skewness and the kurtosis of the distributions. Clearly, these values depend on the resolution of the simulated detectors,

and thus on the aggregation of the events into pixels. In fact, let us recall that we have produced two fundamental datasets, each of 150×150 pixels: the first is \mathcal{D}_{ME} , in which every sample has the statistical moments arising from the maximum number (i.e., 4.5×10^6) of events, whereas the second is \mathcal{D}_{LE} , which has samples whose statistical moments are derived from a smaller number (i.e., 10^5) of events; this entails a reduction of a factor 45 in the volume of the muonic events.

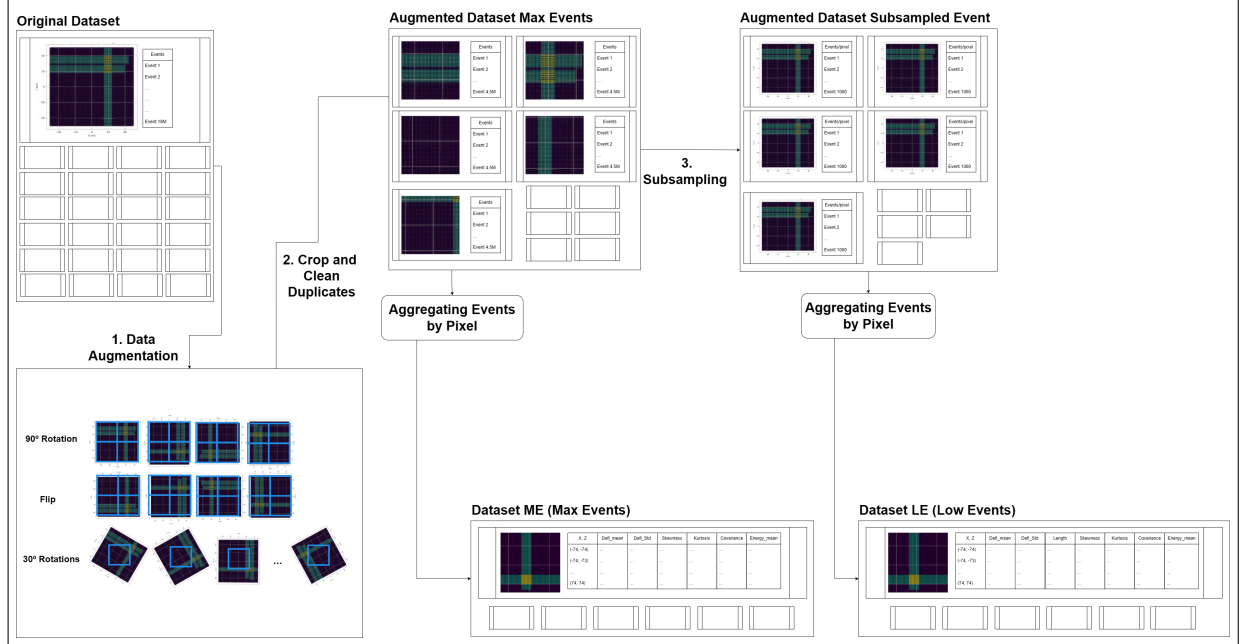


Figure 5: Data augmentation pipeline: the process begins with the original dataset \mathcal{D}_0 , which undergoes data augmentation through rotations and flips to increase diversity. Then, some cropping and duplicate cleaning follow, yielding to the creation of augmented datasets with a maximum number of muon events. Subsequently, a subsampling generates datasets with fewer events, which are used to train neural networks for image reconstruction. As a final step, we proceeded to aggregate the events calculating the statistical moments of the distribution for a resolution of 150×150 pixels. The outcome of this pipeline consists of two datasets: \mathcal{D}_{ME} , in which every sample has the statistical moments arising from a distribution of 4.5×10^6 events, and \mathcal{D}_{LE} , in which every sample has the statistical moments arising from the aggregation of only 10^5 events.

It is here worth remarking that, in order to avoid any possible contamination

between the training data and the test data, we purposed all the samples obtained from the geometries 1 to 50 of the dataset \mathcal{D} generated by GEANT4 only for test, and moreover we confined the training only onto the samples obtained from the geometries 51 to 100 of the dataset \mathcal{D} .

4.2 Neural network architecture

Our neural networks employed a refined U-Net design augmented with residual-in-residual dense blocks (RRDB). The reason for this choice is that RRDB have proven to be effective in various super-resolution and image restoration tasks [25]. Indeed, the chosen architecture makes use of hierarchical feature extraction, and the enhanced feature gets reused in order to produce high-quality reconstructions from the complex input data generated by our GEANT4 simulations.

4.2.1 U-Net architecture with RRDB

The enhanced U-Net architecture consists of an encoder-decoder structure with skip connections, augmented by RRDB in the bottleneck to improve feature extraction and noise suppression. We started setting the U-Net as the baseline architecture, given its ability to handle image-to-image translation tasks through its encoder-decoder symmetry [26]. We should remark that the standard U-Net design is particularly suitable for capturing both global structural information (through encoding at multiple scales) and fine-grained details (via skip connections that reintroduce high-resolution features at later stages). However, we appreciated that standard U-Nets alone may provide unsatisfactory performance when applied to muographic data, which feature subtle and noisy patterns due to low muon statistics [25]. For this reason, we inserted RRDBs, each of which embeds multiple layers of residual dense connections, into the U-Net structure. This allowed the residual dense connections to reuse features and stabilize training while, at the same time, the residual-in-residual structure preserved spatial details with a usually better gradient flow, even in deep networks. Remarkably, this approach gave rise to an improved representational power as well as to a very good capability in dealing with scenarios characterized by a low signal-to-noise ratio. The overall architecture is depicted in Fig. 6.

4.2.2 Detailed network configuration

The modified U-Net architecture with RRDB follows a multi-scale encoder-decoder pathway. Each encoder stage consists of a pair of convolutional layers (with batch

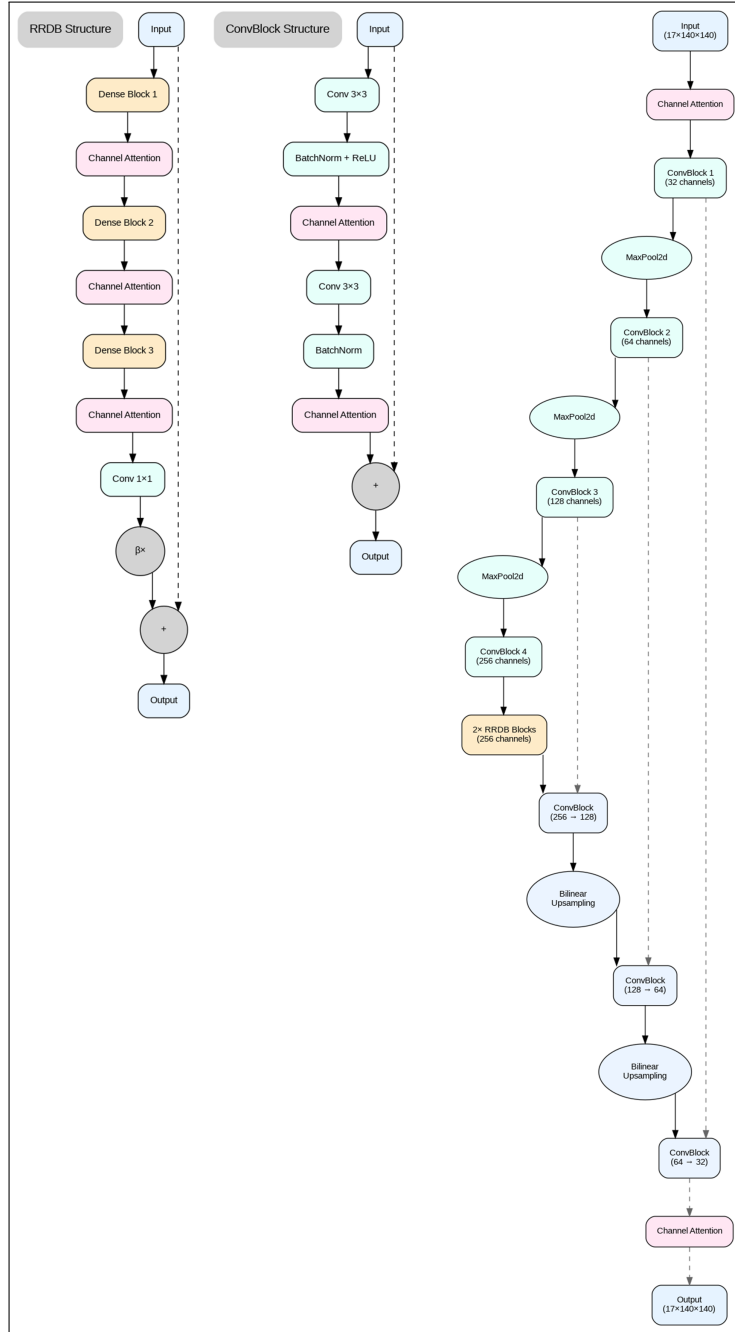


Figure 6: The architecture of our models is a U-Net architecture augmented by RRDB. On the right, one can see the overall architecture, whereas on the left the RRDB and Convolutional blocks are depicted.

normalization and non-linear activation). followed by a spatial downsampling operation (e.g., max pooling). Then, the decoder symmetrically upsample the compressed features back to their original resolution, thereby reintroducing high-level semantic information and merging it with spatially resolved features passed through skip connections from the corresponding encoder stage. The bottleneck of the U-Net was replaced by a sequence of RRDB, as can be seen in the left column of Fig. 6. Each RRDB contains multiple dense blocks connected in a residual-in-residual fashion. These dense blocks stack several convolutional layers, Fig. 7, and each of these layers takes as input all preceding feature maps within the block. This ultimately helps the network to learn increasingly complex representations, while reducing vanishing gradients.

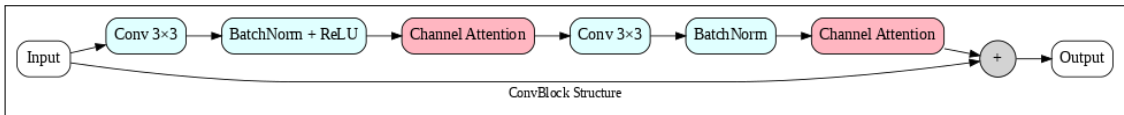


Figure 7: Convolutional block structure used within the U-Net model. The sequence of operations, including convolution, batch normalization, ReLU activation, and channel attention, is depicted.

Encoder and decoder paths. The encoder starts from a set of input feature maps derived from muographic observables. It progressively reduces spatial dimensions, capturing global contextual information, see Fig. 8. Each level consists of convolutional blocks that extract local features, followed by downsampling. Conversely, the decoder receives the transformed, high-level features at the bottleneck and then refines them through successive upsampling. Each decoder stage concatenates the upsampled features with the corresponding encoder features via skip connections, thus reintroducing rich spatial details (which were lost during the downsampling).

Connections and channel attention mechanisms. We have also successfully improved the noise robustness of the network, by making use of channel attention modules [27]. The channel attention weights feature channels based on their relative importance, and they focus the network on the critical aspects of the input data. The embedding of channel attention both within the encoding and

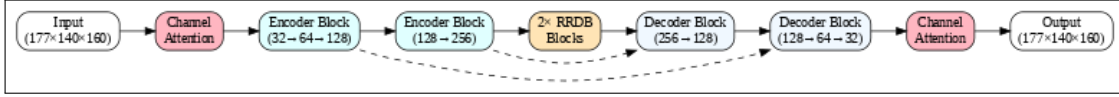


Figure 8: Detailed diagram of the encoder-decoder structure. The encoder path reduces spatial dimensions while extracting high-level features, whereas the decoder restores the spatial resolution, by integrating low-level details.

decoding paths, as well as within the RRDB structured as in Fig. 9, causes the network to emphasize meaningful muon scattering patterns, as well as structural variations in the target object.

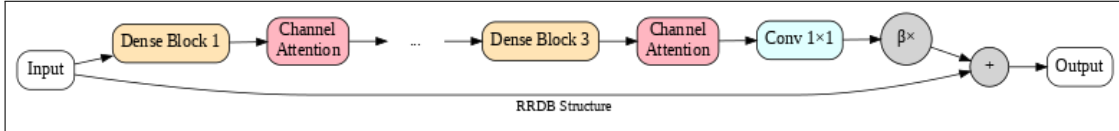


Figure 9: RRDB structure used in the bottleneck of the enhanced U-Net model. The RRDB integrates multiple dense blocks with residual connections.

4.2.3 Hyperparameter selection

Next, we performed a systematic and detailed hyperparameter investigation. Key hyperparameters included the initial learning rate, the number of RRDB, the growth rate within the dense layers, and the choice of the normalization and activation functions. We used AdamW optimizer [28] for a stable convergence, and we also used a learning rate scheduler with early stopping criteria, for computational efficiency and to prevent overfitting.

4.3 Training process

Within our methodological approach, the neural network was always trained to predict the statistics of the dataset with the largest number of events, i.e. \mathcal{D}_{ME} , from the statistical moments of the dataset with the smallest number of events, i.e. \mathcal{D}_{LE} . The training (conducted on a NVIDIA T4 GPU with 16 GB) was then performed onto a different number of geometries, i.e., 5, 20 and 50, with the aim to clearly showing any improvement.

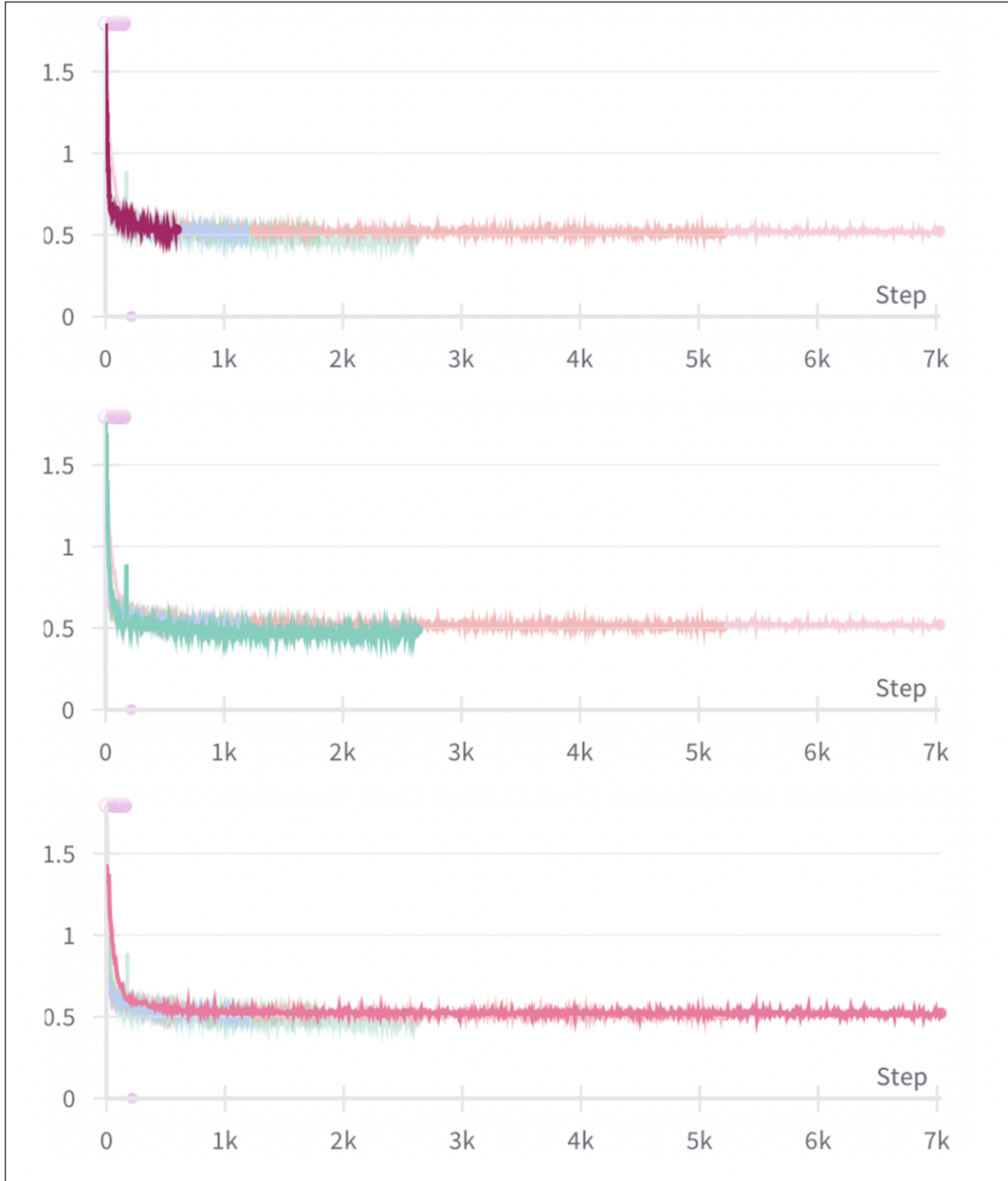


Figure 10: Batch loss comparison across different U-Net models trained on 5, 20 and 50 geometries respectively. One can easily appreciate a rapid decrease of the loss during the initial steps, then stabilizing around 0.5. When compared to others, the model trained with 50 geometries has a slightly lower and more stable loss.

4.3.1 Loss function and optimization algorithm

For the training process we used a L_1 loss function, i.e., the mean absolute error between the predicted and target images. The choice of the L_1 loss function can be motivated by its robust convergence and its effectiveness in determining sharp reconstructions. We also used the AdamW optimizer [28], which features stable convergence properties. During the entire training process, the initial learning rate (LR) was set to a low value (e.g., 10^{-6}), and then gradually increased to its maximum (e.g., 5×10^{-4}). In addition, We also applied gradient clipping, to prevent exploding gradients and to ensure stable updates during the backpropagation.

Training schedule and validation strategy. As for the training schedule, we set 300 as the maximum number of epochs, but we employed an early stopping criterion in which the validation loss does not improve for a certain number of epochs. Additionally, when the validation loss reached a plateau, we reduced the learning rate to achieve better convergence. We always maintained a 80/20 train/validation split, and the validation set was never used for weight updates, but rather it served as a checkpoint to monitor generalization and to guide hyperparametric adjustments.

Computational resources and performance. Training times varied depending on the number of geometries considered: for 5 geometries, training was approximately 1 hour, while 20 geometries took around 4 hours, and 50 geometries requested about 8 hours of runtime. The GPU memory usage remained at about 30%. A graphical representation of the loss during training is given in Fig. 10.

The final trained model has a memory footprint of about 36 MB, and it features very effective inference capabilities, taking on the order of tens of milliseconds per sample.

5 Results

As detailed above, we considered the training on 5, 20 and 50 geometries, leaving all other geometries for testing the models. Compared to the baseline (given by the simple averaging of the muon events, without any deep learning technique), in all three such cases we observed a dramatic gain in the image quality. In fact, we obtained results far beyond our expectations in achieving clearer, higher-resolution images from a significantly lower number of muonic events. In order to

quantify the impact of our setup, we used standard image quality metrics, such as:

- *Peak Signal-to-Noise Ratio* (PSNR): higher PSNR indicates cleaner reconstructions and less noise.
- *Structural Similarity Index Measure* (SSIM): quantifies structural resemblance between reconstructed and target images, with values closer to 1 indicating more faithful reconstructions [29].
- *Gradient Magnitude Similarity Deviation* (GMSD): this evaluates the sharpness of the reconstructed images [30]. Lower values indicate that edges and gradients are preserved more faithfully.

5.1 Analysis of the quality metrics

Considering that neural network training aims to predict statistics for a larger number of muonic events (specifically, predict the statistics of the \mathcal{D}_{ME} dataset, corresponding to 4.5×10^6 events, starting from the statistics of the \mathcal{D}_{LE} dataset obtained with 10^5 events), we measured the above quality metrics on 10 geometries not included among those used for training. For each of such 10 geometries, the metrics were evaluated by comparing the results of the baseline (i.e., the statistics of \mathcal{D}_{LE}), the predictions made with the model trained on 5 geometries (5G), on 20 geometries (20G), and on 50 geometries (50G), with the statistics obtained with the maximum number of events (i.e., the statistics of \mathcal{D}_{ME}).

As it can be realized at a glance from Fig. 11, the baseline has a significantly lower PSNR and SSIM compared to the processed images with models trained on 5, 20 or 50 geometries; we recall that the PSNR measures the quality of reconstructed images by quantifying the error between the reconstructed image and the target image (higher PSNR values correspond to lower reconstruction errors). On the other hand, the SSIM focuses on structural and perceptual similarity. On both of these metrics, the model trained on 20 geometries achieves the best compromise between the highest PSNR and SSIM values and low variability. On the other hand, the increasing of the dataset size to 50 geometries does not seem to yield to any substantial improvements on these metrics, whereas the variability seems to increase, hinting at a possible overfitting of the model.

The case of the GMSD is trickier, since this is an edge-based metric which evaluates the similarity of the gradients between images; thus, when the GMSD is

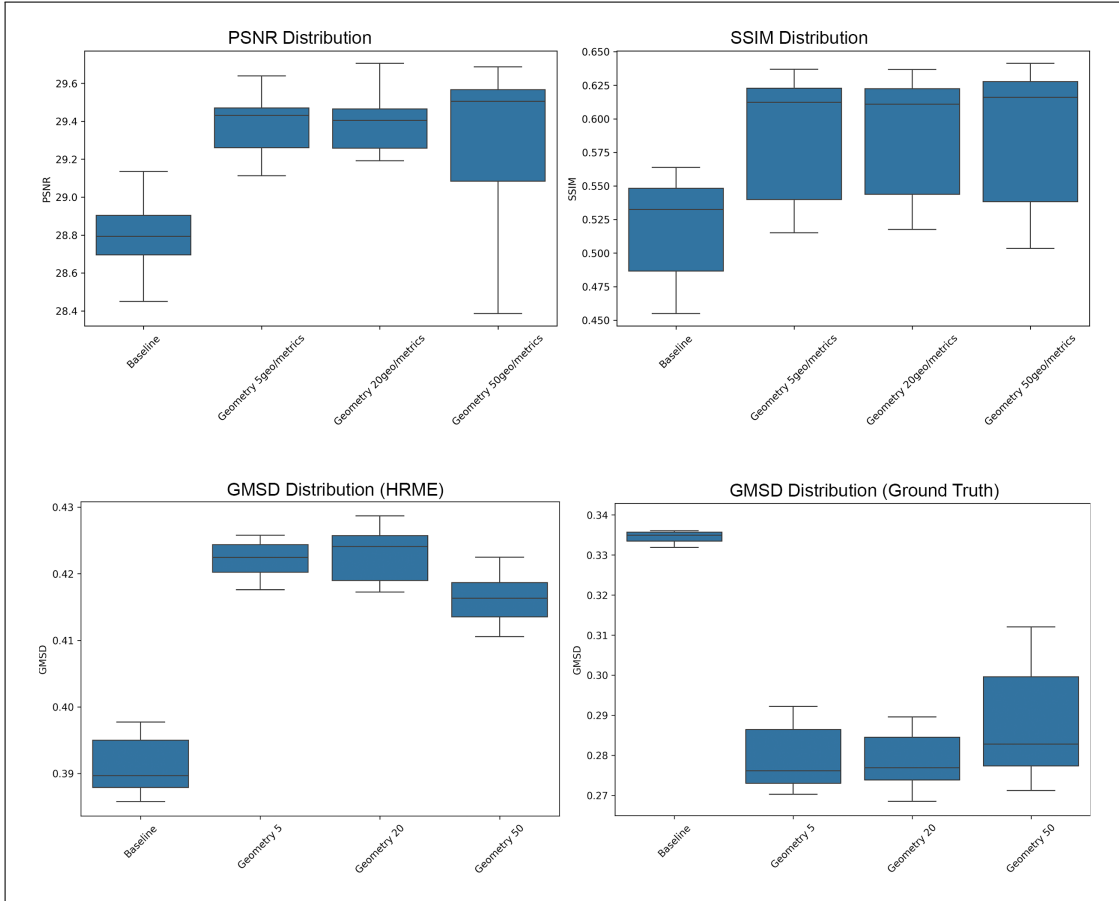


Figure 11: Distribution of the performance metrics across different neural network training setups. The top left panel shows the PSNR distribution, whose higher values indicate an improved image quality and a reduced noise. The top right panel reports the SSIM distribution, reflecting how well the predicted images preserve the structural details compared to the ground truth. The bottom left panel depicts the distribution of the GMSD pertaining to the \mathcal{D}_{ME} dataset, for which lower values indicate better edge preservation. Finally, the bottom right panel shows the distribution of the GMSD measured against the Ground Truth; it can be easily appreciated that the models trained on 20 and 50 geometries achieve closer similarity to the ideal image, when compared to the baseline as well as to models trained on 5 geometries.

lower, the edges are better preserved. Unlike the above metrics, we noticed that, as far as the GMSD is concerned, the baseline model significantly outperformed

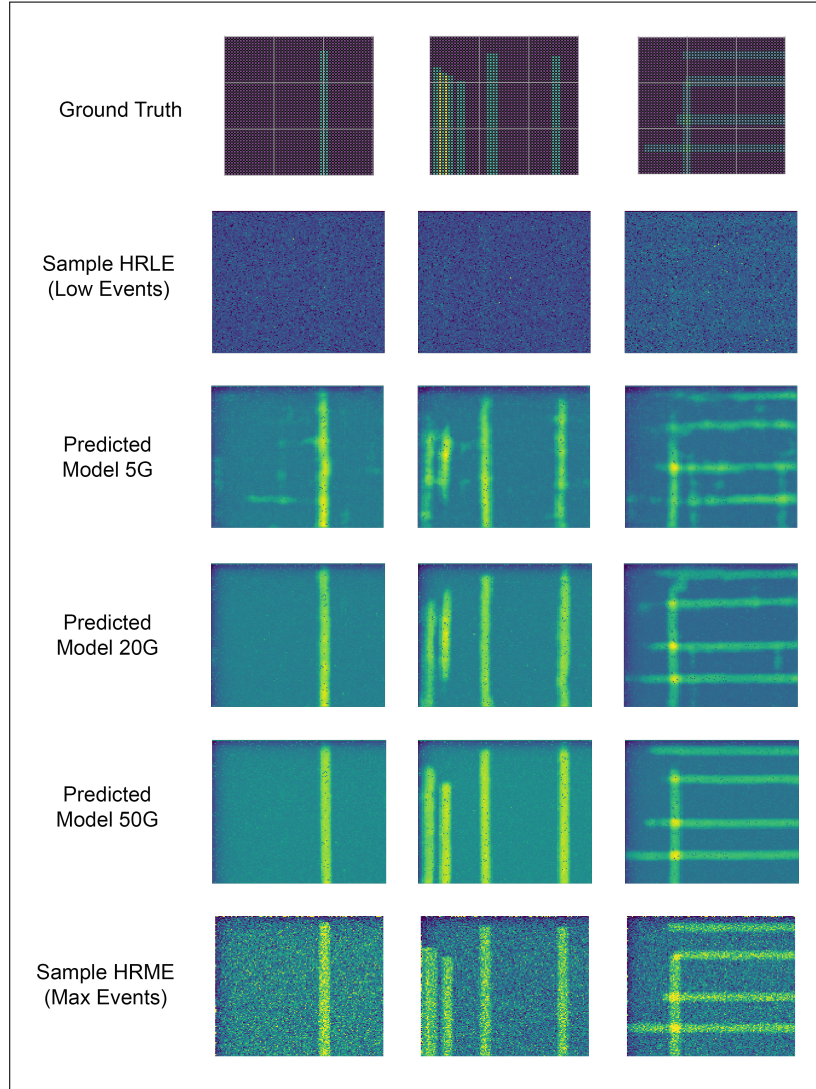


Figure 12: Ground truth, \mathcal{D}_{LE} sample (Low Events), predicted samples and \mathcal{D}_{ME} sample (Max Events) sample of Geometries 20, 21 and 27. In the first row is represented the Ground Truth with an image obtained directly from the material budget of the geometry. The second row is given by the respective samples from the \mathcal{D}_{LE} dataset (Low Events, i.e. obtained with 10^5 events). In the following three rows, we see the predicted images by the models trained on 5, 20, and 50 geometries, respectively. Finally, in the last row one finds the corresponding samples from the \mathcal{D}_{ME} dataset (obtained with 4.5×10^6 events).

the others (Fig. 11, bottom left). This can ultimately be traced back to the presence of a strong noise in the muonic statistics, which is considered to be a meaningful detail from the GMSD; for this reason, we decided to proceed with an additional evaluation of the images with the Ground Truth image, directly obtained by calculating the material budget (Fig. 11, bottom right). As expected, the GMSD of the predicted images with respect to the Ground Truth is definitely better than the one of the baseline, and this provides a non-trivial confirmation that the prediction models not only enhance the meaningful structure of the image, but they also reduce the noise. Overall, the results regarding the GMSD metric are in line with the trends observed above for the PSNR and the SSIM; this provides further evidence to the statement that the model trained with 20 geometries achieves the most consistent performance.

5.2 Visual comparisons and qualitative analysis

Regardless of the statistical metrics, significant conclusions can be drawn simply by visualizing the results. In Fig. 12, one can see the three geometries, with a representation of the material budget (Ground Truth) shown in the first row, and followed by the respective samples from the \mathcal{D}_{LE} dataset (low events obtained with 10^5 events), which are then used as input for the neural networks. In the subsequent three rows, one can see the images predicted by the models trained on 5, 20, and 50 geometries, respectively, and finally the corresponding samples from \mathcal{D}_{ME} dataset (obtained with 4.5×10^6 events). It can be easily realized that the readability of the image greatly improves when switching from the one obtained with the statistics of 10^5 muonic events to the one obtained with the statistics pertaining to any of the three models trained on 5, 20 or 50 geometries. Notwithstanding the aforementioned fact that the quantitative metrics tend to single out the model trained on 20 geometries as the best, the visual analysis indicates that (with a small difference) the image obtained with the model trained on 50 geometries is noticeably better. This conclusion can be confirmed by the analysis of the null case, Fig. 13: from the latter figure, it can be appreciated that the model trained on 5 geometries actually introduced some artifacts, which got then reduced within the model trained on 20 geometries, and further completely removed in the image obtained from the predicted statistics of the model trained on 50 geometries.

Fig. 14 highlights the differences between the input statistics and those resulting from the predictive models. Its first column reports the image obtained

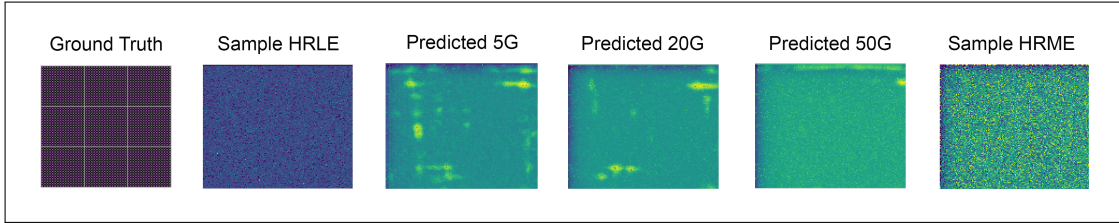


Figure 13: Ground truth, \mathcal{D}_{LE} sample, predicted samples and \mathcal{D}_{ME} sample of geometry 26, which is also a null case. As one can see, the model trained on 5 geometries introduced some artifacts, which were then reduced resp. almost completely removed by the model trained on 20 resp. 50 geometries.

from the statistics of the sample from the Low Event dataset, i.e. \mathcal{D}_{LE} , whereas its second column hosts the image obtained from the predicted models trained on 5, 10 and 20 geometries, respectively. Finally, in the third column one can see the image resulting from the difference between the input sample and the predicted samples. It is plain to see that the difference between the two statistics is of paramount relevance for visual understanding of the structure of the analysed geometry.

6 Conclusion

In this work, we investigate the possible application of a new method, integrating GEANT4 simulations and advanced deep learning models, to improve the efficiency of data acquisition in muon tomography (muography) applied to reinforced concrete structures.

By performing detailed radiation-matter interaction simulations, we showed that the reconstruction of high-resolution images of typical iron support elements (of 1 cm thickness) inside 30 cm-deep concrete blocks can be achieved successfully, solely relying on analytical methods. Additionally, through the use of convolutional neural networks, particularly U-Net architectures enhanced with residual-in-residual dense blocks (RRDB), we were able to reconstruct high-resolution images from datasets with a significantly lower number of muon events.

Deep learning models, trained on synthetic datasets generated by detailed GEANT4 simulations, have significantly improved the quality of the reconstructed images, while simultaneously reducing noise and amplifying the structural features of the images themselves. Surely, the effectiveness in the detection and visualiza-

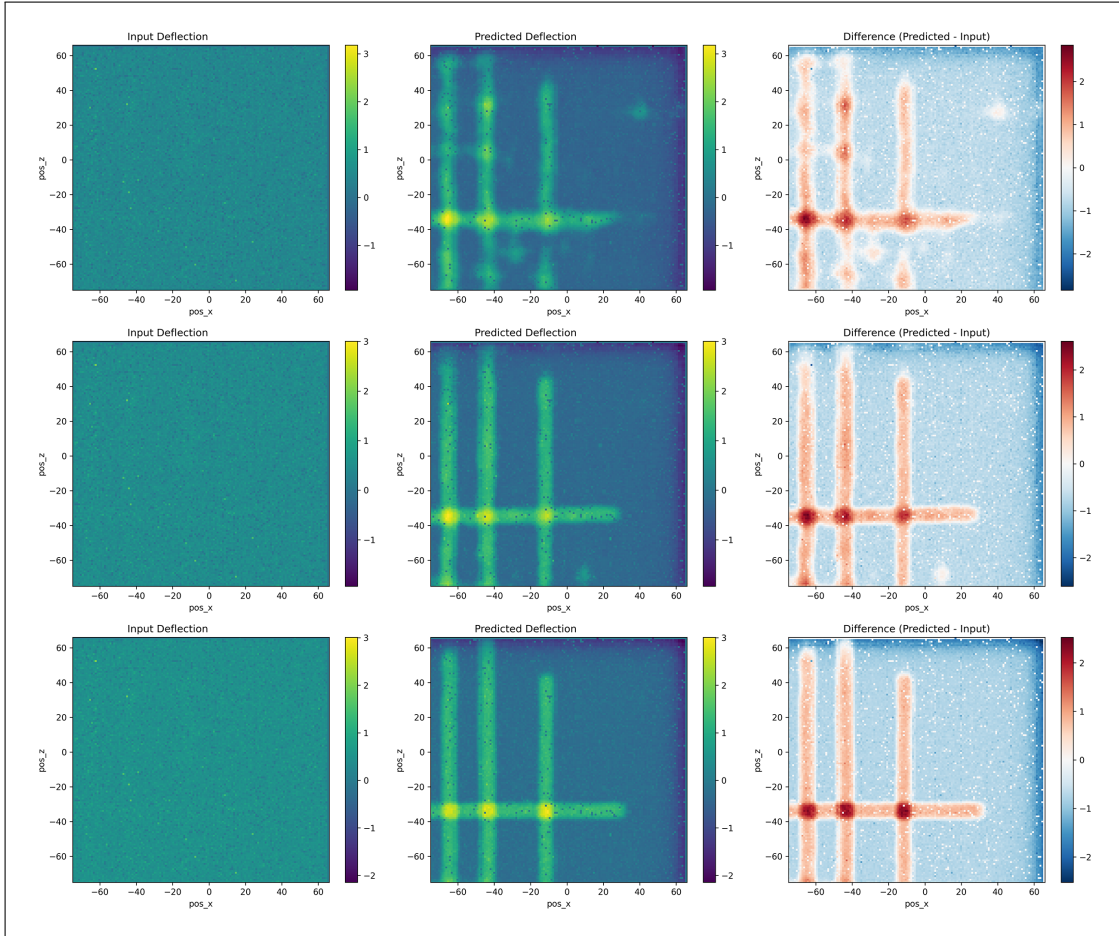


Figure 14: The first column reports the image obtained from the statistics of the sample from the Low Event dataset, i.e. \mathcal{D}_{LE} , of geometry 11. On the second column, one can see the image obtained from the predicted models trained on 5, 10 and 20 geometries, respectively. Finally, the third column reports the image resulting from the difference between the input sample and the predicted sample.

tion of internal metallic components in the concrete, even with a reduced number of muon events, represents an important step forward for the practical application of muography in structural diagnostics.

The comparative analysis of models trained on datasets of different sizes (5, 20, and 50 geometries) indicates that, although all models show improvements over the baseline, a network trained on 20 geometries suffices in demonstrating

a good balance between performance and computational efficiency: this model achieves superior PSNR, SSIM, and GMSD metrics; nevertheless, we should not refrain from remarking that a visual inspection seems to single out the results of the model trained on 50 geometries as the best ones, resulting in greater image clarity, as well as in a reduction of artifact formation as the dataset size increases.

Directions for future developments can be drawn quite clearly from the present study. Just to name a few, one could use a muon distribution similar to that present in nature for cosmic muons, or also test the proposed method on some real muographic data, with the aim to validate the generalization capacity of the trained models.

All in all, the present investigation lays the foundation for an effective exploitation of muography into routine civil engineering inspections, providing a powerful, non-invasive tool, capable of detecting internal structural anomalies with unprecedented and unparalleled depth and resolution. The reduction of the data acquisition times and the substantial improvement of the image quality are other two crucial features of our method, which could possibly result in more frequent and cost-effective assessments of critical infrastructures, thus contributing to improve their safety, as well as to extend their lifetime.

Acknowledgments

We would like to thank STAP - Reabilitação Estrutural s.a. for its support to this research.

References

- [1] Z.X. Zhang, T. Enqvist, M. Holma and P. Kuusiniemi, “*Muography and its potential applications to mining and rock engineering*”, *Rock Mechanics and Rock Engineering* (2020) 1–15. [P. 3]
- [2] L.W. Alvarez, J.A. Anderson, F.E. Bedwei, J. Burkhard, A. Fakhry, A. Girgis, A. Goneid, F. Hassan, D. Iverson, G. Lynch et al., “*Search for Hidden Chambers in the Pyramids. The structure of the Second Pyramid of Giza is determined by cosmic-ray absorption*”, *Science* **167** (1970), n. 3919, 832–839. [P. 3]
- [3] K. Morishima, M. Kuno, A. Nishio, N. Kitagawa, Y. Manabe, M. Moto, F. Takasaki, H. Fujii, K. Satoh, H. Kodama et al., “*Discovery of a big void in Khufu’s Pyramid by observation of cosmic-ray muons*”, *Nature* **552** (2017), n. 7685, 386–390. [P. 3]
- [4] L. Cimmino, G. Baccani, P. Noli, L. Amato, F. Ambrosino, L. Bonechi, M. Bongi, V. Ciulli, R. D’Alessandro, M. D’Errico et al., “*3D muography for the search of hidden cavities*”, *Scientific Reports* **9** (2019), n. 1, 2974. [P. 3]
- [5] H.K. Tanaka, T. Uchida, M. Tanaka, M. Takeo, J. Oikawa, T. Ohminato, Y. Aoki, E. Koyama and H. Tsuji, “*Detecting a mass change inside a volcano by cosmic-ray muon radiography (muography): First results from measurements at Asama volcano, Japan*”, *Geophysical Research Letters* **36** (2009), n. 17,. [P. 3, 4]
- [6] H.K. Tanaka, “*Subsurface density mapping of the earth with cosmic ray muons*”, *Nucl. Phys. B, Proc. Suppl.* **243** (2013) 239–248. [P. 3]
- [7] V. Tioukov, A. Alexandrov, C. Bozza, L. Consiglio, N. D’Ambrosio, G. De Lellis, C. De Sio, F. Giudicepietro, G. Macedonio, S. Miyamoto et al., “*First muography of Stromboli volcano*”, *Scientific Reports* **9** (2019), n. 1, 6695. [P. 3]
- [8] K.N. Borozdin, G.E. Hogan, C. Morris, W.C. Priedhorsky, A. Saunders, L.J. Schultz and M.E. Teasdale, “*Radiographic imaging with cosmic-ray muons*”, *Nature* **422** (2003), n. 6929, 277–277. [P. 3]

- [9] C. Thomay, J. Velthuis, T. Poffley, P. Baesso, D. Cussans and L. Frazão, “*Passive 3D imaging of nuclear waste containers with muon scattering tomography*”, *Journal of Instrumentation* **11** (2016), n. 03, P03008. [P. 3]
- [10] E. Niederleithinger, Y. Guangliang, D. Mahon and S. Gardner, “*Muon tomography applied to assessment of concrete structures: First experiments and simulations*”, in *Proceedings of NDT-CE 2022*, pp. 1–8, NDT.net (2022). [P. 3, 4]
- [11] International Atomic Energy Agency (IAEA), “*Muon Imaging. Present Status and Emerging Applications*”, in *IAEA-TECDOC-2012*, pp. 1–116, IAEA TecDoc Series (2012). [P. 3]
- [12] C. Wang, M. Beer and B.M. Ayyub, “*Time-dependent reliability of aging structures: Overview of assessment methods*”, *ASCE-ASME J. Risk Uncertain. Eng. Syst. A* **7** (2021), n. 4, 03121003. [P. 3]
- [13] S. Chen, C. Duffield, S. Miramini, B.N.K. Raja and L. Zhang, “*Life-cycle modelling of concrete cracking and reinforcement corrosion in concrete bridges: A case study*”, *Engineering Structures* **237** (2021) 112143. [P. 3]
- [14] Structural Engineering Institute, “*Guideline for Structural Condition Assessment of Existing Buildings*”; American Society of Civil Engineers, Reston, Virginia (2000). [P. 3]
- [15] ACI Committee 562, “*Assessment, Repair, and Rehabilitation of Existing Concrete Structures - Code and Commentary*”; American Concrete Institute, Farmington Hills, USA (2019). [P. 3]
- [16] C. Maierhofer, “*Nondestructive Evaluation of Concrete Infrastructure with Ground Penetrating Radar*”, *Journal of Materials in Civil Engineering* **15** (2003) 287–297. [P. 3]
- [17] S.K. Verma, S.S. Bhadauria and S. Akhtar, “*Review of nondestructive testing methods for condition monitoring of concrete structures*”, *Journal of Construction Engineering* **2013** (2013), n. 1, 834572. [P. 3]
- [18] H.K. Tanaka, C. Bozza, A. Bross, E. Cantoni, O. Catalano, G. Cerretto, A. Giammanco, J. Gluyas, I. Gnesi, M. Holma et al., “*Muography*”, *Nature Reviews Methods Primers* **3** (2023), n. 1, 88. [P. 4]

- [19] Particle Data Group et al., “*Review of Particle Physics*”, *Prog. Theor. Exp. Phys.* **2020** (2020), n. 8, 083C01. [P. 4]
- [20] S. Agostinelli, J. Allison, K.a. Amako, J. Apostolakis, H. Araujo, P. Arce, M. Asai, D. Axen, S. Banerjee, G. Barrand et al., “*Geant4 – A simulation toolkit*”, *Nucl. Instrum. Methods Phys. Res. A* **506** (2003), n. 3, 250–303. [P. 4, 6]
- [21] J. Allison, K. Amako, J. Apostolakis, H. Araujo, P.A. Dubois, M. Asai, G. Barrand, R. Capra, S. Chauvie, R. Chytracsek et al., “*Geant4 developments and applications*”, *IEEE Trans. Nucl. Sci.* **53** (2006), n. 1, 270–278. [P. 4, 6]
- [22] J. Allison, K. Amako, J. Apostolakis, P. Arce, M. Asai, T. Aso, E. Bagli, A. Bagulya, S. Banerjee, G. Barrand et al., “*Recent developments in Geant4*”, *Nucl. Instrum. Methods Phys. Res. A* **835** (2016) 186–225. [P. 4, 6]
- [23] Z. Wei, Y. Huang, Y. Chen, C. Zheng and J. Gao, “*A-ESRGAN: Training real-world blind super-resolution with attention U-Net Discriminators*”, in *Pacific Rim International Conference on Artificial Intelligence*, (Singapore), pp. 16–27, Springer, 2023. [P. 5]
- [24] Q. Chen, H. Li and G. Lu, “*Training ESRGAN with multi-scale attention U-Net discriminator*”, *Scientific Reports* **14** (2024), n. 1, 29036. [P. 5]
- [25] X. Wang, K. Yu, S. Wu, J. Gu, Y. Liu, C. Dong, Y. Qiao and C. Change Loy, “*ESRGAN: Enhanced Super-Resolution Generative Adversarial Networks*”, in *Computer Vision – ECCV 2018 Workshops*, pp. 63–79, Springer International Publishing, Cham (2019). [P. 15]
- [26] O. Ronneberger, P. Fischer and T. Brox, “*U-Net: Convolutional Networks for Biomedical Image Segmentation*”, in *Medical Image Computing and Computer-Assisted Intervention*, pp. 234–241, Springer, Cham (2015). [P. 15]
- [27] J. Hu, L. Shen and G. Sun, “*Squeeze-and-Excitation Networks*”, in *Proceedings of the IEEE Conference on Computer Vision and Pattern Recognition*, pp. 7132–7141 (2018). [P. 17]
- [28] I. Loshchilov and F. Hutter, “*Decoupled Weight Decay Regularization*”, in *7th International Conference on Learning Representations*, OpenReview.net (2019). [P. 18, 20]

- [29] Z. Wang, A.C. Bovik, H.R. Sheikh and E.P. Simoncelli, “*Image quality assessment: From error visibility to structural similarity*”, IEEE Trans. Image Process. **13** (2004), n. 4, 600–612. [P. 21]
- [30] W. Xue, L. Zhang, X. Mou and A.C. Bovik, “*Gradient magnitude similarity deviation: A highly efficient perceptual image quality index*”, IEEE Trans. Image Process. **23** (2014), n. 2, 684–695. [P. 21]